

Band offsets in cubic GaN/AlN superlattices

C. Mietze,¹ M. Landmann,² E. Rauls,² H. Machhadani,³ S. Sakr,³ M. Tchernycheva,³
F. H. Julien,³ W. G. Schmidt,² K. Lischka,¹ and D. J. As¹

¹*Experimentalphysik, Universität Paderborn, Warburger Strasse 100, D-33098, Germany*

²*Lehrstuhl für Theoretische Physik, Universität Paderborn, Warburger Strasse 100, D-33098, Germany*

³*Institut d'Electronique Fondamentale, UMR 8622 CNRS, University Paris-Sud 11, F-91405 Orsay, France*

(Received 30 November 2010; revised manuscript received 17 March 2011; published 4 May 2011)

The presently unknown band offset in nonpolar cubic GaN/AlN superlattices is investigated by inter-sub-band and interband spectroscopies as well as *ab initio* calculations. On one hand, the conduction-band offset (CBO) has been determined from the comparison of the measured transition energies with model calculations within the effective mass approximation. On the other hand, the valence-band offset (VBO) and the CBO are accurately simulated by calculating many-body corrections within the *GW* approximation on top of hybrid-functional density functional theory calculations. Thus, a CBO of (1.4 ± 0.1) eV and a VBO of (0.5 ± 0.1) eV is obtained as a result of both approaches.

DOI: [10.1103/PhysRevB.83.195301](https://doi.org/10.1103/PhysRevB.83.195301)

PACS number(s): 78.67.Pt, 73.21.Cd, 81.15.Hi, 71.15.Mb

I. INTRODUCTION

One of the most crucial parameters that determines the physics in heterostructures and for the optimization and design of optoelectronic devices, based on, e.g., quantum wells (QWs), is the electronic band alignment at the interface between two semiconductors. More precisely, one is interested in the valence-band offset (VBO) and the conduction-band offset (CBO), which reflect how the band-gap difference of the involved semiconductor materials is portioned between the discontinuities of the occupied and unoccupied energy bands. Due to their technological importance, the band offsets between various semiconductor alloys have been subjected to extensive experimental and computational studies. Today, group-III nitrides are the materials of choice for manifold device applications, such as light-emitting diodes (LEDs), laser diodes, or field-effect transistors. Based on the large band discontinuity between AlN, GaN, and InN, novel nitride devices based on inter-sub-band transitions (ISBTs), such as quantum well infrared photodetectors (QWIPs) or quantum cascade lasers operating at telecommunication wavelengths are proposed.¹

State-of-the-art group-III nitrides crystallize in the stable wurtzite structure. This hexagonal phase is characterized by strong internal piezoelectric and pyroelectric fields along the *c* axis, which are undesirable for many optoelectronic applications. In multi-QWs or superlattices (SLs), these internal fields complicate the design and limit the tunability of ISBT energies. In polar group-III nitride QWs, the transition energy is observed to be almost independent of the well width for thick wells due to the confinement of carriers in a triangular potential caused by the internal field. The growth of nonpolar and semipolar nitrides has found increasing interest in the past years to avoid these strong internal fields. In these nonpolar (semipolar) nitrides, the *c* axis is orthogonal (inclined) to the growth direction, eliminating the field effects in the growth direction. The absence of these internal fields leads to an increased transition probability and, therefore, to enhanced luminescence intensity and reduced shift in emission wavelength in LEDs. However, the electrical, optical, and structural properties show strong lateral anisotropy since the

polarization field is now in the plane of growth. Furthermore, due to the large anisotropic biaxial stress, relaxation and cracking of AlGaIn in one direction are observed.

An alternative way to fabricate group-III nitrides without spontaneous polarization fields is the growth of metastable nonpolar cubic (c) group-III nitrides.² Zinc-blende GaN, InN, and AlN epilayers and just recently, free-standing GaN substrates have been successfully synthesized using plasma-assisted molecular-beam epitaxy (PA-MBE).^{2,3} Especially, the determination of optimal growth conditions for nonpolar c-GaN (Ref. 4) and c-AlN (Ref. 5) has pushed the development of electronic and optoelectronic devices, such as heterojunction field-effect transistors,⁶ resonant tunneling diodes,⁷ and QWIPs⁸ based on zinc-blende group-III nitrides. Furthermore, the tunability of ISBTs from mid- to far-infrared regions in cubic GaN/AlN SLs has been shown.⁹

ISBTs give direct access to the CBO. The ISBT energy for a fixed QW structure depends only on the barrier height or the CBO between well and barrier material. Hence, the CBO can be used as a fitting parameter in model calculations of ISBT energies based on an effective mass model.

The *ab initio* access to the band alignment at heterostructure interfaces is directly related to referring the calculated energy levels in an extended solid to a well-defined energy reference. The average electrostatic potential of an infinite bulk crystal is an ill-defined constant,^{10,11} but it is a well-defined quantity for the interface of two semi-infinite solids. This property was used by Baldereschi *et al.*¹⁰ to split the VBO $\Delta E_v^{(A,B)}$ of two semiconductors *A* and *B* into two terms according to

$$\Delta E_v^{(A,B)} = \Delta \overline{V}_{el}^{(A/B)} + \Delta E_{vbm}^{(A,B)}. \quad (1)$$

Here, $\Delta \overline{V}_{el}^{(A/B)}$ is the shift in the macroscopic average of the electrostatic potential across the interface of a semiconductor-alloy heterostructure. Usually, it is obtained from *ab initio* calculations of periodic SLs within the supercell approach. Thus, all effects of strain due to the epitaxial growth on a substrate and electronic relaxations and/or redistributions at the heterostructure's interface are included in the first term. The second contribution, $\Delta E_{vbm}^{(A,B)}$, is the difference between

the valence-band maxima of the bulk materials calculated separately for both semiconductors A and B . Based on Eq. (1), the CBO $\Delta E_c^{(A,B)}$ may be obtained by adding the difference $\Delta E_g^{(A,B)}$ of the fundamental bulk band gaps of the semiconductor materials A and B ,

$$\Delta E_c^{(A,B)} = -\Delta E_v^{(A,B)} + \Delta E_g^{(A,B)}. \quad (2)$$

In this paper, we report on the optical characterization of nonpolar c-GaN/AlN SL structures by inter-sub-band absorption and photoluminescence (PL) measurements. *Ab initio* calculations are performed to accurately determine the VBO. Combining the results of the *ab initio* calculations with the experimental data of the ISBT and interband transition, a CBO-to-VBO ratio of $74(\pm 5):26(\pm 5)$ is obtained.

This paper is organized as follows: Sec. II describes the methodological approaches of the underlying experimental and computational frameworks. In Sec. III, we present and discuss the results of the particular methods. Finally, Sec. IV is used for a summary and a comparative discussion of experimental and theoretical results.

II. METHODOLOGY

A. Experiment and model calculations

Our samples were grown by PA-MBE on 10- μm -thick 3C-SiC substrates on top of Si (100) (NovaSiC). Two series of samples were fabricated. Samples of series A consist of a 100-nm c-GaN buffer followed by a 20-period GaN/AlN SL. The active region is capped by a 100-nm GaN layer. The AlN thickness varied between 1.3 and 1.7 nm, and the GaN QW thickness varied between 2.0 and 2.5 nm. In the second series of samples (series B), the number of SL periods was extended to 40. The AlN barrier thickness was 3.0 nm, and GaN QW thickness was varied from 1.8 to 5.0 nm. The cap layer was 7-nm thick. Growth rates of the different layers were observed *in situ* by reflection high-energy electron diffraction intensity oscillations. The strain of the samples was determined using high-resolution x-ray diffraction (HRXRD). A modification of the band gap due to strain can be calculated using Eqs. (3) and (4),

$$E_{\text{gap, strained}} = E_{\text{gap, 0}} + 2a_c \left(1 - \frac{c_{12}}{c_{11}} \right) \epsilon_{xx}, \quad (3)$$

$$\epsilon_{xx} = \frac{a_{\text{GaN}}}{a_{\text{AlN}}} - 1. \quad (4)$$

Here, $E_{\text{gap, strained}}$ is the band-gap energy of the strained layer, $E_{\text{gap, 0}}$ is the band-gap energy of the bulk material, a_c is the deformation potential, and c_{11} and c_{12} are the elastic constants. ϵ_{xx} is the misfit between GaN and AlN with the lattice parameters a_{AlN} and a_{GaN} . The thicknesses of the single layers were verified by simulations of HRXRD data based on dynamical scattering theory.¹²

Inter-sub-band spectroscopy is performed with a Fourier transform infrared spectrometer. Two opposite facets of the samples were optically polished at an angle of 30° in order to allow multiple passes in the active layers when irradiating the input facet at normal incidence. Interband spectroscopy is performed using a HeCd laser (325 nm) as the excitation

TABLE I. Parameters used for transition energy calculations.

Parameter	c-AlN	c-GaN
$E_{\text{gap, 300 K}}$ (eV)	5.3 ^a	3.2 ^b
a (\AA)	4.38 ^c	4.52 ^c
m_{hh}^*/m_0	1.2 ^d	0.8 ^d
m_{lh}^*/m_0	0.33 ^d	0.18 ^d
m_e/m_0	0.19 ^d	0.13 ^d
a_c (eV)	-6.8 ^e	-2.77 ^e
c_{11} (GPa)	304 ^e	296 ^e
c_{12} (GPa)	152 ^e	156 ^e
E_p (eV)	23.84 ^f	16.86 ^f
F		0.6
Δ (eV)		0.017 ^g

^aReference 19.

^bReference 20.

^cReferences 21 and 22.

^dReferences 23 and 24.

^eReferences 25 and 26.

^fReference 27.

^gReference 28.

source. A Spex 270M monochromator combined with a GaAs photomultiplier and a Hamamatsu C3866 photon counter were used to detect emitted light from the SL samples.

Model calculations based on a single-band effective mass model with periodic boundary conditions using nextnano³ (Ref. 13) are performed to obtain theoretical ISBT energies. More detailed information on nextnano³ can be found in Refs. 14 and 15. For all QW samples, an enhancement of effective masses due to nonparabolicity effects is also taken into account. In thin GaAs/AlAs QWs, it has been shown that the effective electron masses increase with decreasing well width.¹⁶ For all samples, the energy dependency of the effective electron mass is calculated using a modified Kane formula,^{17,18}

$$\frac{m_0}{m^*(\epsilon)} = 1 + 2F + \frac{E_p}{3} \left(\frac{2}{E_g + \epsilon} + \frac{1}{E_g + \Delta + \epsilon} \right). \quad (5)$$

Here, ϵ is the confinement energy of the lowest sub-band, E_p is the interband matrix element, F accounts for coupling to remote bands, and Δ is the spin-orbit splitting of the valence band. The value of F was assumed to be 0.6 so that the effective mass for zero confinement energy results in the bulk value. The parameters of c-GaN and c-AlN used for these calculations are given in Table I. Then, the CBO is used as a fitting parameter to achieve optimal agreement between calculated and measured ISBT energies.

B. *Ab initio* calculations

We have performed density functional theory (DFT) calculations^{29,30} using the projector-augmented wave (PAW) method^{31,32} as implemented in the Vienna *Ab initio* Simulation Package (VASP).³³ An energy cutoff of 400 eV was used throughout this paper to expand the Kohn-Sham orbitals into plane-wave basis sets. Within the DFT approach, the electronic band structure of semiconductors, and, therefore, the band gap, depends on the choice of the exchange correlation (XC) functional. Therefore, we applied both the local-density

approximation (LDA)^{34,35} and the nonlocal screened Coulomb potential hybrid density functionals [Heyd-Scuseria-Ernzerhof (HSE)].^{36–39} The LDA functional is well known to significantly underestimate semiconductor band gaps or even to predict zero band gaps for small-gap semiconductors in some cases.^{38,40} This is among other reasons due to a missing derivative discontinuity^{41,42} and an incomplete self-interaction cancellation^{35,43} in the LDA XC potential.

The mixing of a notable amount of nonlocal Hartree-Fock (HF) exchange interaction in so-called hybrid functionals [e.g., PBE0 (Refs. 44–47)] has proven to improve the description of the electronic structure (i.e., band gaps). Most of the computational difficulties of this approach arise from the evaluation of the slowly decaying Fock exchange E_X^{HF} (also called exact exchange) with distance, which is why the use of traditional hybrid functionals is avoided for large systems.^{36,37} In consideration of this problem, Heyd *et al.*³⁶ proposed a more tractable hybrid-functional scheme for extended systems.

In general, the HSE-type functional exhibits the form

$$E_{\text{XC}}^{\text{HSE}} = \alpha E_X^{\text{HF,SR}}(\mu) + (1 - \alpha) E_X^{\text{PBE,SR}}(\mu) + E_X^{\text{PBE,LR}}(\mu) + E_C^{\text{PBE}}. \quad (6)$$

Here, α defines the percentage of Fock exchange included, and μ is the actual controlling parameter for the range separation of the exchange interaction into short-range (SR) and long-range (LR) components. The correlation energy E_c remains unchanged with respect to the Perdew-Burke-Ernzerhof (PBE)⁴⁸ functional. In agreement with the original definitions,^{36,37,39,49} we refer to the parameter values $\alpha = 0.25$, $\mu = 0.3 \text{ \AA}^{-1}$ as HSE03 and to $\alpha = 0.25$, $\mu = 0.2 \text{ \AA}^{-1}$ as HSE06, respectively. In some calculations, we changed the amount of exact exchange in Eq. (6) from its standard value $\alpha = 0.25$. In these cases, the applied functional is labeled by mod(α)HSE03/06. So far, DFT HSE-functional calculations with similar settings have been successfully applied to molecules,³⁶ extended crystals,^{50,51} and defect levels.⁵²

Besides the hybrid-functional approach, which basically developed from the observation of reverse errors in the electronic structure in classic DFT and HF calculations,⁵³ many-body perturbation theory (MBPT) offers a way to include many particle interactions beyond the single-particle mean-field theories. A successful approximation within MBPT^{54,55} is Hedin's GW approximation^{56,57} for independent quasiparticles (QPs). Within the GW approximation,⁵⁸ QP energies $E_{n\mathbf{k}}^{\text{QP}}$, as measured in photoabsorption and photoemission spectroscopies, are solutions to a set of nonlinear equations containing the nonlocal energy-dependent self-energy operator $\Sigma(r, r', E_{n\mathbf{k}}^{\text{QP}})$ instead of the Kohn-Sham XC functional,

$$(T + V_{\text{ext}} + V_H - E_{n\mathbf{k}}^{\text{QP}}) \Psi_{n\mathbf{k}}(\mathbf{r}) + \int d^3\mathbf{r}' \Sigma(r, r', E_{n\mathbf{k}}^{\text{QP}}) \Psi_{n\mathbf{k}}(\mathbf{r}') = 0. \quad (7)$$

The self-energy is obtained as a convolution of the single-particle Green's function G and the dynamically screened

Coulomb interaction W , which is constructed from the polarization propagator in random-phase approximation,⁵⁵

$$\Sigma(r, r', \omega) = \frac{i}{4\pi} \int_{-\infty}^{\infty} d\omega' e^{i\omega'\delta} G(\mathbf{r}, \mathbf{r}', \omega + \omega') W(\mathbf{r}, \mathbf{r}', \omega'). \quad (8)$$

In principle, these QP equations should be solved self-consistently by updating QP wave functions and QP energies.

In practice, the lowest-order non-self-consistent GW results are obtained from application of first-order perturbation theory to the results of computationally less demanding DFT calculations. The first-order energy corrections (so-called QP shifts) $\Delta E_{n\mathbf{k}}^{\text{QP}}$ are given by

$$\Delta E_{n\mathbf{k}}^{\text{QP}} = \langle n\mathbf{k} | \Sigma - V_{xc}^{\text{DFT}} | n\mathbf{k} \rangle, \quad (9)$$

where the perturbation is given by the difference between the self-energy and the DFT XC functional.

Generally, this single shot GW strategy is known as the G_0W_0 approach. G_0W_0 systematically improves band gaps with a remaining underestimation tendency of experimental values.⁵⁹ Besides non-self-consistent G_0W_0 calculations, partially self-consistent schemes for G or W and fully self-consistent schemes for G and W have been applied to selected problems.^{60,63} However, especially for the full update of G and W , a significant overestimation of electronic band gaps is observed for some materials (e.g., GaAs, GaN).⁶⁰ We calculated QP corrections for the bulk materials by various frequency-dependent GW schemes on top of LDA and HSE calculations.

The GW calculations for primitive bulk unit cells were carried out with 240 electronic bands, 200 frequency grid points for sampling the dielectric function, and a regular Γ -centered $8 \times 8 \times 8$ k-point mesh. The Brillouin-zone integration of heterostructure-unit cells was performed using a $12 \times 12 \times 2$ Monkhorst-Pack k-point sampling⁶⁴ in LDA-PBE calculations and a regular Γ -centered $8 \times 8 \times 2$ k-point mesh in HSE calculations. The k-point grid was down-sampled by a factor of 2 to evaluate the Fock exchange in the HSE heterostructure calculation.

All calculations treated the 3d electrons of Ga as valence states within the PAW potentials.

The heterostructure-unit cell (cf. Fig. 1) represents a periodic array of 1.8-nm (eight layers) c-GaN and 1.6-nm (eight layers) c-AlN slabs. In detail, the unit cell has been constructed to match the experimental structure of the pseudomorphically grown SL with a strained c-AlN lattice matched to the c-GaN substrate system. Therefore, the experimental value $a_{\text{exp}}^{\text{GaN}} = 4.52 \text{ \AA}$ (Ref. 22) has been chosen for the in-plane and out-of-plane lattice constants of the GaN part as well as for the in-plane lattice constant of AlN. The out-of-plane lattice constant of the AlN slab $a_{z, \text{GaN}} = 4.12 \text{ \AA}$ has been determined with respect to volume conservation of the strained material. A structural relaxation of the AlN out-of-plane lattice constant on the LDA level results in exactly the same value. Additionally, we performed calculations with a fully optimized out-of-plane lattice constant in the whole unit cell and in-plane lattice constants fixed to the optimized DFT (LDA, PBE) lattice constants of GaN and AlN ($a_{\text{GaN}}^{\text{LDA}} = 4.46 \text{ \AA}$, $a_{\text{GaN}}^{\text{PBE}} = 4.54 \text{ \AA}$, $a_{\text{AlN}}^{\text{LDA}} = 4.35 \text{ \AA}$, $a_{\text{AlN}}^{\text{PBE}} = 4.40 \text{ \AA}$) to estimate the influence of

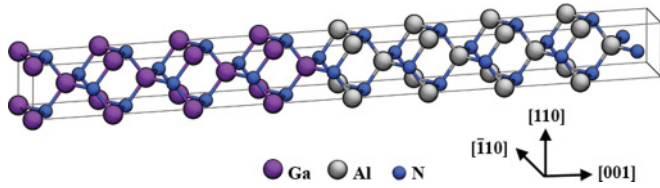


FIG. 1. (Color online) Unit cell of the pseudomorphically strained $(\text{GaN})_8(\text{AlN})_8(001)$ heterostructure.

lattice relaxations on the potential steps and band offsets (cf. Table IV). For the bulk-unit cells, the experimental lattice constants $a_{\text{GaN}} = 4.52 \text{ \AA}$ and $a_{\text{AlN}} = 4.38 \text{ \AA}$ were used.^{22,65,66}

The potential shifts $\Delta \bar{V}_{el}(z)$ across the growth direction z of the SL have been estimated by performing a two-step averaging procedure on the local electrostatic potential. First, a microscopic planar average over the lattice periodic directions x and y (i.e., $[110]$, $[\bar{1}10]$, cf. Fig. 1) has been calculated according to

$$\bar{V}_{el}(z) = \frac{1}{A_{\text{cell}}} \int dx dy V_{el}(x, y, z). \quad (10)$$

In a second step, the remaining rapid bulklike oscillations (cf. Fig. 2) have been averaged out by

$$\begin{aligned} \bar{\bar{V}}_{el}(z) = \int dz' dz'' \omega_{\text{GaN}}(z - z') \\ \times \omega_{\text{AlN}}(z - z') V_{el}(x, y, z''), \end{aligned} \quad (11)$$

with

$$\omega_{\text{GaN,AlN}}(z) = \frac{1}{2d_{\text{GaN,AlN}}} \Theta(d_{\text{GaN,AlN}} - |z|). \quad (12)$$

Here, $d_{\text{GaN,AlN}}$ are the growth-direction interlayer distances of the *c*-GaN and strained *c*-AlN bulk materials, and Θ is the Heaviside function.

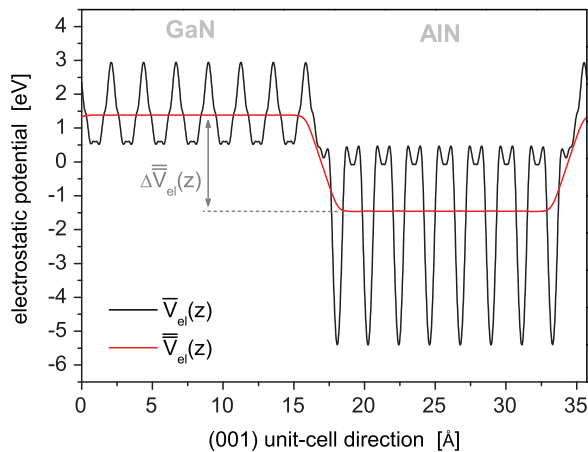


FIG. 2. (Color online) Microscopic planar average $\bar{V}_{el}(z)$ and macroscopic average $\bar{\bar{V}}_{el}(z)$ of the local electrostatic potential of the pseudomorphic GaN/AlN heterostructure. The local electrostatic potential was determined from a DFT-LDA calculation with PAW pseudopotentials and Ga *d* electrons treated as valence states.

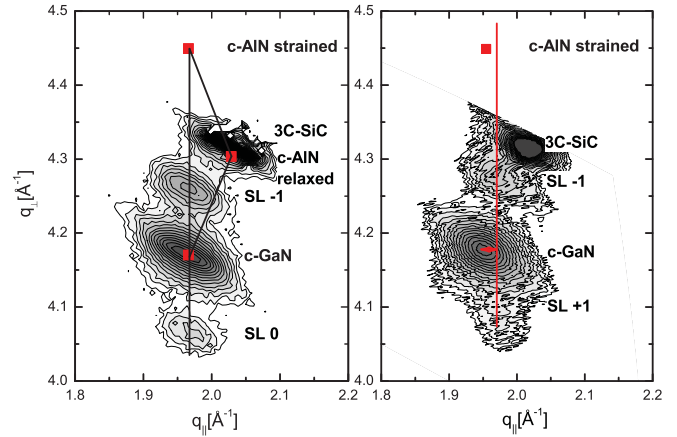


FIG. 3. (Color online) RSMs of samples A3 (left) and B2 (right) revealing strain in the SL structures. The SL in sample A3 is pseudomorphically strained to the GaN buffer while sample B2 shows partial relaxation.

III. RESULTS AND DISCUSSION

A. Experiment and model calculations

In the following paragraphs, the results of structural and optical characterizations and model calculations are summarized. The structural properties are characterized in Sec. III A 1. In Sec. III A 2, the results of inter-sub-band and interband spectroscopies are depicted. A detailed description of the model calculation results is given in Sec. III A 3.

1. Structural properties

The HRXRD reciprocal space maps (RSMs) of the asymmetric (113) reflection of samples A3 (left) and B2 (right) are shown in Fig. 3.

Both RSMs reveal two SL satellites, the reflexes of the substrate and the buffer and cap layers. As can be seen in the left-side diagram, the SL satellites have the same q_{\parallel} like the *c*-GaN. We conclude that the SLs are pseudomorphically grown on the *c*-GaN buffer for series A, resulting in strained AlN barriers. The AlN layers are tensile strained to the GaN buffer due to the smaller lattice parameter of AlN with respect to GaN. As a result of the tensile strain, we find a reduction of the band-gap energy of the AlN of about 0.2–5.1 eV [see Eq. (3)]. The right diagram shows that the SL satellites do not have the same q_{\parallel} as the *c*-GaN. Thus, we conclude that the SL is partially relaxed (maximum 30%) due to the higher total volume of AlN for series B. This partial relaxation results in an additional modification of the band gaps of well and barrier. The modified band gaps are 3.23 eV for GaN and 5.15 eV for AlN. These small modifications result in a change in ISBT energy, for example, less than 10 meV for sample B3 and, therefore, are neglected for further considerations. The structural properties of the samples are summarized in Table II.

2. Optical properties

Figure 4 shows normalized inter-sub-band absorption spectra of all samples under TM-polarized light. The spectra are fitted by Gaussian functions. The absorption spectra for series

TABLE II. Structural properties of the SLs obtained from HRXRD measurements and simulations.

Sample	d_{GaN} [nm]	d_{AlN} [nm]
A1	2.0	1.3
A2	2.2	1.3
A3	2.5	1.7
B1	5.0	3.0
B2	3.0	3.0
B3	1.8	3.0

A are taken from Ref. 67. Most of the spectra show oscillations from Fabry-Pérot interferences in the 10- μm -thick 3C-SiC layer. The absence of these oscillations for samples A1 and A3 is explained by larger interface roughnesses between 3C-SiC and Si. As shown in Fig. 4, all samples exhibit inter-sub-band absorption with a peak energy in the range of 0.3–0.9 eV. Furthermore, the absorption spectra of series B show a smaller full width at half maximum (FWHM) than series A. This may be explained by the thicker AlN barriers. AlN shows a tendency to smaller roughness and smooth interfaces.⁵

The measured PL spectra of our samples are plotted in Fig. 5.

From these, spectra transition energies of interband transitions from the lowest conduction-band level to the highest valence-band level are obtained. The FWHM of the PL lines is increasing with increasing PL transition energy, since the effect of monolayer (ML) thickness fluctuations is increasing with decreasing well width.

3. Model calculations

The ISBT and interband transition energies in our SLs are calculated with an effective mass model using nextnano.³ From Eq. (5), we obtain a maximum effective electron mass of 0.15 m_0 for the largest confinement energy.

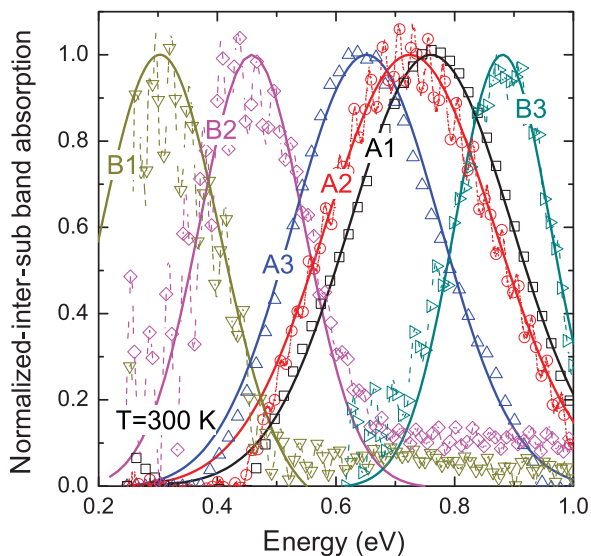


FIG. 4. (Color online) Normalized room-temperature inter-sub-band absorption spectra (symbols) fitted with Gaussian functions (lines).

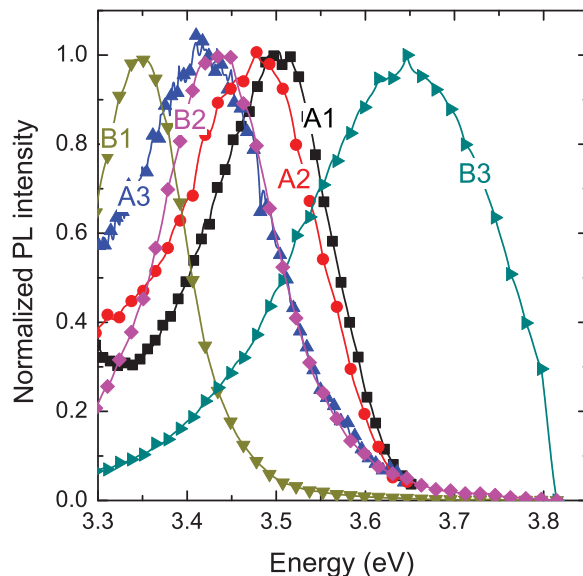


FIG. 5. (Color online) Normalized room-temperature PL spectra.

Figure 6 shows a comparison between measured and calculated ISBT energies. The symbols represent the experimental data. For fixed well and barrier widths, the CBO is one parameter that influences the ISBT energy. For our samples, we varied the CBO between 1.0 and 1.7 eV, which corresponds to a ratio of $\Delta E_c : \Delta E_v$ between 50:50 and 90:10, respectively. The curves in Fig. 6 are calculated ISBT energies and are plotted versus the CBO. First, we see that the transition energy dependency on the CBO is increasing with decreasing well width and higher confinement energies consequently. Therefore, the samples with higher ISBT energies provide higher reliability of the determined CBO. We find good agreement for all samples assuming a CBO of 1.4 ± 0.1 eV

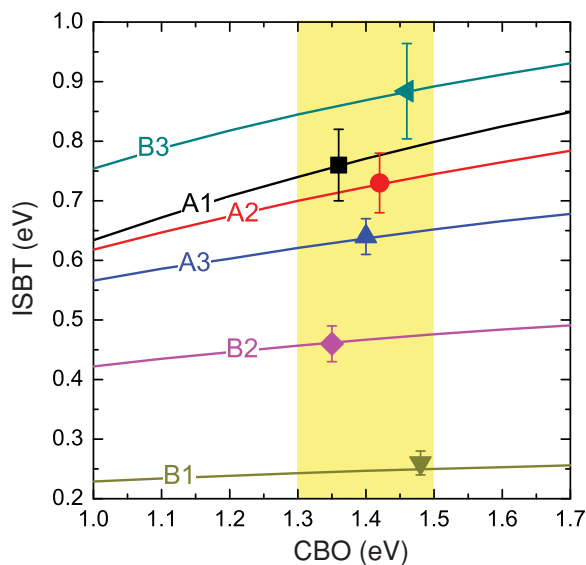


FIG. 6. (Color online) Calculated ISBT energy for different CBOs (lines) in comparison to experimental values (symbols). The bars indicate the calculated variation of the transition energy for a variation of the well width of ± 1 ML.

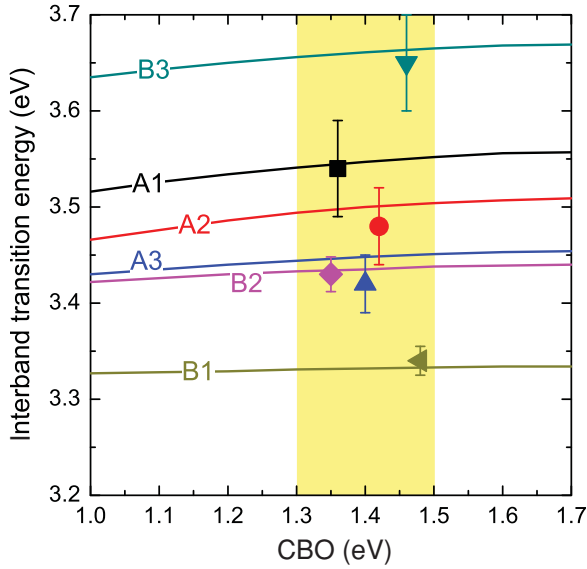


FIG. 7. (Color online) Calculated interband transition energy for different CBOs (lines) in comparison to experimental values (symbols). The bars indicate the calculated variation of the transition energy for a variation of the well width of ± 1 ML.

resulting in $(74 \pm 5)\%$ of the band-gap differences ΔE_{gap} between GaN and AlN.

In Fig. 7, we compare calculated and measured interband transition energies. These studies verify the results of the ISBT investigations. All samples show good agreement within the uncertainty resulting from a variation of the calculated transition energy for a variation of the well width of ± 1 ML. The band-offset dependency of the interband transition energy is larger for thinner QWs, e.g., samples A1, A2, A3, and B3. This results in smaller slopes of the calculated curves for thick QWs (B1, B2) than in thin QWs. Furthermore, we find that a 1-ML fluctuation in QW thickness results in a larger change of transition energy for thinner QWs. All experimental data show good agreement with our calculations based on the preliminarily determined band offsets and effective masses from inter-sub-band spectroscopy. In addition, a fluctuation in layer thickness of more than 1 ML cannot be excluded for larger well widths.

In summary, comparison of experimental ISBT and interband transition energies with model calculations gives evidence for a CBO in the range of 1.4 ± 0.1 eV. This value differs from experimental values for the hexagonal system where a CBO of 1.7 eV is found.⁶⁸ Although the local structure and bonding are very similar for both systems, there are significant differences. In contrast to our indirect c-AlN, the wurtzite AlN is a direct semiconductor with a 0.7-eV larger band gap.⁶⁹ Furthermore, the band gap of c-GaN is 0.19-eV smaller than in hexagonal GaN.²⁰ This may explain the differences in band offsets, although the local structure is very similar.

B. *Ab initio* calculations

In this section, we report and discuss the results of our *ab initio* calculations with the focus on band gaps, potential shifts, and band offsets.

TABLE III. Calculated band gaps of c-GaN and c-AlN. Approximations for the XC functional in the DFT calculation and the used *GW* methods are given in the first and second columns. For c-AlN, the direct and indirect band gaps are listed. Reported experimental values are $E_{\text{gap}}^{\text{GaN}}(\Gamma - \Gamma) = 3.3$ eV, $E_{\text{gap}}^{\text{AlN}}(\Gamma - \Gamma) = 5.9$ eV, and $E_{\text{gap}}^{\text{AlN}}(\Gamma - X) = 5.3$ eV.

XC	Method	GaN			AlN	
		$(\Gamma - \Gamma)$	$(\Gamma - \Gamma)$	$(\Gamma - X)$	$(\Gamma - \Gamma)$	$(\Gamma - X)$
LDA		1.67	4.15	3.22		
LDA	G_0W_0	2.95	5.71	4.83		
LDA	GW_0	3.13	6.00	5.13		
LDA	<i>GW</i>	3.46	6.48	5.61		
PBE		1.66	4.12	3.31		
HSE03		2.70	5.25	4.32		
HSE03	G_0W_0	3.45	6.28	5.31		
HSE03	GW_0	3.55	6.44	5.47		
HSE03	<i>GW</i>	3.73	6.70	5.73		
HSE06		2.92	5.50	4.56		
HSE06	G_0W_0	3.54	6.37	5.40		
mod(30)HSE06	-	3.19	5.78	4.82		
mod(30)HSE06	G_0W_0	3.65	6.50	5.52		

1. Band gaps

The results of our band-gap calculations for c-GaN and c-AlN bulk materials carried out on the different levels of theory are summarized in Table III. Reported experimental reference values are $E_{\text{gap}}^{\text{GaN}}(\Gamma - \Gamma) = 3.3$ eV (Ref. 66), $E_{\text{gap}}^{\text{AlN}}(\Gamma - \Gamma) = 5.9$ eV (Ref. 19), and $E_{\text{gap}}^{\text{AlN}}(\Gamma - X) = 5.3$ eV (Ref. 19). The (semi)local XC functionals, LDA and PBE, perform equally bad and underestimate the band gaps of GaN by almost a factor of 2 and the indirect gap of AlN by 2 eV. We should note that the similarity of LDA and PBE values is due to the usage of experimental lattice constants in the bulk calculations. Differences in other calculations^{70,71} are mainly due to different equilibrium lattice constants, obtained from an optimization of the supercell volume using LDA or PBE functionals. A significant improvement of band gaps on the DFT level is obtained by inclusion of exact exchange in the form of HSE-type functionals for both materials. For HSE03/HSE06, the GaN-gap underestimation is reduced to 0.6 eV/0.38 eV, and in the case of a modified exact-exchange percentage of 30% [cf. Eq. (6)], the underestimation of the experimental value is minimized to 0.11 eV. For AlN, the HSE functionals still underestimate the indirect band gap significantly. The best value for the indirect gap of 4.82 eV again, is obtained for an increased amount of Fock exchange but is still approximately half an eV too small. This behavior of HSE-type functionals exemplarily demonstrates the characteristics of this approach. Medium-sized band-gap materials (such as GaN) are reasonably described in HSE03 and HSE06. Especially, the band gap may be tuned to match the experiment by slight modifications of the exact-exchange fraction. In addition, the HSE06 functional tends to describe the midgap semiconductors slightly better than HSE03. In contrast to medium band-gap materials, band gaps of wide-gap semiconductors (such as AlN) cannot be described accurately by HSE-type functionals using a reasonable (i.e., universally

applicable) amount of exact exchange. The description of wide-gap materials should rather tend to the HF limit instead of showing significant screening properties that are described by HSE. Accordingly, a general HSE-DFT problem arises if, as in this study, midgap and wide-gap semiconductor-material properties are mixed up in a single system. In this case, the constant amount of Fock exchange cannot be changed in a way that both subsystems are described equally well.

The band-gap results for the various GW approaches exhibit a rather heterogeneous picture. Starting from DFT-LDA wave functions, the midgap material GaN is best described in a partially (LDA + GW_0) or fully (LDA + GW) self-consistent GW approach. In LDA + GW_0 , W is fixed to its initial DFT value W_0 , and G is repeatedly iterated a fixed number of steps or until self-consistency. In this paper, G is iterated four times with respect to the QP eigenvalues, which has proven to produce reliable QP energies.^{72,73} The LDA + GW_0 band gap of 3.13 eV underestimates the measured value by 0.17 eV, which is comparable to the mod(30)HSE06 result without QP corrections. In LDA + GW calculations, W is iterated in the same way as G (i.e., four times). Since the iteration of G and W increases the band gap, the GaN band-gap underestimation is turned into almost the same overestimation of 0.16 eV. A single shot G_0W_0 correction to the LDA eigenvalues still suffers from an significant band-gap underestimation by 0.35 eV. These trends change by going to the HSE functional. Starting from HSE03 wave functions, an almost identical to LDA + GW GaN band gap is obtained in HSE03 + G_0W_0 . HSE06 + G_0W_0 and mod(30)HSE06 + G_0W_0 tend to increase this overestimation. The GW_0 and GW calculations on top of the HSE03 calculation lead to an even stronger overestimation of the band gap by 0.25 and 0.43 eV.

For the wide-gap semiconductor AlN, the HSE + G_0W_0 approach gives reliable indirect band gaps that are within ± 0.2 eV of the experimental value. In HSE03 + G_0W_0 , the calculated band gap of 5.31 eV is almost identical to the experimental value. On the LDA + G_0W_0 level, the DFT underestimation is not completely compensated by G_0W_0 QP shifts. In the partially self-consistent GW_0 scheme, the LDA result is significantly improved. The HSE03 GW_0 result shows a slight band-gap overestimation that becomes significantly worse in the self-consistent GW procedure with updated G and W . This self-consistency problem has been traced back to be mainly due to the neglect of vertex corrections⁶⁰ (i.e., electron-hole interaction) in the self-consistent independent QP (GW) approaches.

In conclusion, the best description of the common GaN/AlN system may be obtained by performing single shot G_0W_0 calculations on top of a HSE-type calculation obtained with a screening parameter and an exact-exchange percentage that represent the best compromise for describing both materials. In general, one could expect that the original HSE03/HSE06 parameters are the best choice in preparation of a G_0W_0 calculation. The conceptual and pragmatistical advantages of this approach are that the best DFT wave functions (i.e., the wave functions closest to the QP wave functions) are used in a traditional first-order perturbation theory approach, thereby avoiding the necessity to think about corrections to the self-consistent GW cycle. Nevertheless, if self-consistency

TABLE IV. Calculated shifts of the macroscopically averaged electrostatic potential $\bar{V}_{el}(z)$ [cf. Eq. (11)] of pseudomorphically strained and various DFT-optimized (GaN)₈(AlN)₈(001) heterostructure-unit cells (cf. Fig. 1).

In-plane lattice constant	Electrostatic potential $\bar{V}_{el}(z)$ [eV]		
	$a_{\text{exp}}^{\text{GaN}}$	$a_{\text{DFT}}^{\text{GaN}}$	$a_{\text{DFT}}^{\text{AlN}}$
LDA	3.12	2.82	2.84
PBE	2.71	2.81	2.83
HSE03	2.69		
HSE06	2.66		

is desirable (as for QP corrections to LDA results), the combination of an iterated G and screening on the DFT level via W_0 leads to quite accurate results. This is due to a surprisingly good description of screening properties on the DFT level. Finally, we have to note that there is a significant overestimation of the reported experimental value for the direct AlN ($\Gamma - \Gamma$) gap, despite the accurate description of the indirect ($\Gamma - X$) gap.

2. Potential shifts

In Table IV, the shifts in the macroscopically averaged electrostatic potential across the heterostructure interface $\bar{V}_{el}(z)$, as defined in Eq. (11), are summarized. Obviously, the potential shifts across the pseudomorphic (GaN)₈(AlN)₈(001) unit cells are very similar for PBE- and HSE-type functionals. The actual difference between the PBE and the HSE potential shifts is < 0.1 eV. These results indicate a similar description of structural properties of the c-group-III nitrides by PBE and HSE (i.e., the PBE equilibrium lattice constant is $a_{\text{GaN}}^{\text{PBE}} = 4.54$ Å and the HSE value is $a_{\text{GaN}}^{\text{HSE}} = 4.52$ Å as reported in Ref. 38). Since HSE-type calculations on the extended heterostructure-unit cells are computationally extremely demanding, therefore, it is a well-justified practice to use the DFT-PBE result to align the energy levels of the separate bulk calculations. Moreover, the self-consistent computation of the local electrostatic potential on the HSE level demonstrates one eminent advantage of the HSE approach. The HSE functionals allow a self-consistent calculation of the electronic structure in contrast to the perturbative GW implementations. Relaxing the heterostructure-unit cells in the growth direction yields a potential shift of 2.82 ± 0.02 eV. This potential shift is almost independent of the XC functional (LDA or PBE) and the particular supercell's in-plane lattice constant. The typical potential-step differences between growth-direction-optimized and pseudomorphic unit cells are about 0.2 eV with the exception of the LDA result. The larger deviation of the LDA value is due to the fact that the experimental lattice constant $a_{\text{GaN}} = 4.52$ Å, used to construct the pseudomorphic unit cell, leads to an atomic structure that is closer to the PBE energy minimum than to the LDA minimum ($a_{\text{GaN}}^{\text{LDA}} = 4.46$ Å).

3. Band offsets

Our QP VBOs and QP CBOs calculated from the fundamental band gaps in Table III, the potential shifts in

TABLE V. DFT and QP VBOs [Eq. (1)] and CBOs of the pseudomorphic (GaN)₈(AlN)₈(001) heterostructure (cf. Fig. 1). The last column lists the $\Delta E_c:\Delta E_v$ ratios.

XC functional	GW method	Band offsets [eV]		Ratio
		ΔE_v	ΔE_c	
LDA		0.73	0.82	53:47
LDA	G_0W_0	0.91	0.98	52:48
PBE		0.37	1.28	78:22
PBE	G_0W_0	0.54	1.32	71:29
HSE03		0.43	1.20	74:26
HSE03	G_0W_0	0.58	1.29	69:31
HSE06		0.42	1.22	74:26
HSE06	G_0W_0	0.56	1.31	70:30
Experimental ^a		0.5 ± 0.1	1.4 ± 0.1	74(±5):26(±5)

^aThis paper.

Table IV, and the corresponding valence-band maxima are listed in Table V. As discussed for the band gaps, we focus on the G_0W_0 approach to QP energies. The QP-band alignment, on the LDA + G_0W_0 , HSE06, and HSE06 + G_0W_0 levels of theory, is additionally depicted in Fig. 8. All our calculations unambiguously predict, in agreement with the experiment, a type-I SL-band alignment between the c phases of the III-V semiconductor materials GaN and AlN. Most obviously, the obtained HSE and HSE + G_0W_0 VBOs are significantly smaller than the LDA values. The main reason for this difference is, as described in Sec. III B 2, the larger potential shift at the interface in LDA calculations, which is mainly due to the pseudomorphically strained SL unit used in our calculations. Taking a fully structural relaxation of the GaN/AlN SL into account, with an in-plane lattice constant fixed to the optimized LDA lattice constant of GaN (see Table IV), the resulting VBO/CBO is 0.43 eV/1.12 eV and 0.61 eV/1.28 eV by inclusion of G_0W_0 QP corrections. By doing the same for the PBE functional, we obtain a VBO/CBO of 0.47 eV/1.18 eV and 0.64 eV/1.22 eV with QP corrections. Therefore, the LDA and PBE functionals lead to very similar results for SLs that are not artificially strained. In the same way, these values are closer to the HSE results. Analyzing the G_0W_0 results, a general trend for calculated QP energies is observable. Besides the band gaps, the single shot G_0W_0 QP

shifts also affect the valence-band maxima of GaN and AlN differently. In agreement with previous studies,⁷⁴ this leads to a slight increase (≤ 0.2 eV) of the VBOs. For LDA, the VBO increases by 0.18 eV, for HSE functionals, the VBOs increase by about 0.15 eV.

We note that our LDA and LDA + G_0W_0 band offsets of the pseudomorphic structure are comparable to other reported values by various authors for zinc-blende GaN/AlN SLs. Albanesi *et al.*⁷⁵ obtained a VBO of 0.85 eV using a linear muffin-tin orbital method. Wei and Zunger⁷⁶ obtained a similar value of 0.84 eV using a DFT-LDA method. A larger DFT-LDA result of 0.98 eV has been reported by Binggeli *et al.*⁷⁷ for a GaN/AlN SL pseudomorphically strained to the AlN lattice constant. Cociorva *et al.*⁷⁴ calculated G_0W_0 corrections on top of a DFT-LDA approach and obtained a VBO/CBO of 0.76 eV/0.78 eV for an optimized SL unit cell with a GaN in-plane lattice constant. Altogether, the LDA-based results are, compared to our experimental results, clearly inferior to the HSE-based calculations with and without many-body corrections. Besides the VBOs, the remarkable quality of the HSE-functional calculations is evident by looking at the band-offset ratio $\Delta E_c:\Delta E_v$. The experimental band-offset ratio of 74(±5):26(±5) is well reproduced by the HSE-type XC functionals. Moreover, calculated QP-band offsets tend to predict a very similar 70:30 ratio. The most accurate VBO and CBO ($\Delta E_v = 0.56$ eV and $\Delta E_c = 1.31$ eV) are obtained by HSE06 + G_0W_0 calculations.

One concluding comment on CBOs and the predictive capability of *ab initio* band-offset calculations: Calculated by DFT-related methods, the CBOs always reflect the methods ability to describe unoccupied electronic states. Therefore, results on the LDA/PBE-DFT level, suffering from the serious band-gap underestimation, are not reliable for predicting CBOs. For the considered material system, our hybrid-functional DFT calculations, especially with the inclusion of many-body corrections, allow the calculation of CBOs, with relevant predictive power (i.e., within a relative error of ~ 0.1 eV for the band offsets and an absolute error of ~ 0.2 eV for the band gaps). The present calculations further indicate that standard DFT results using the LDA or PBE functionals are less reliable for predicting VBOs than hybrid functionals. Nevertheless, to establish general trends in the description of semiconductor band offsets by hybrid functionals with

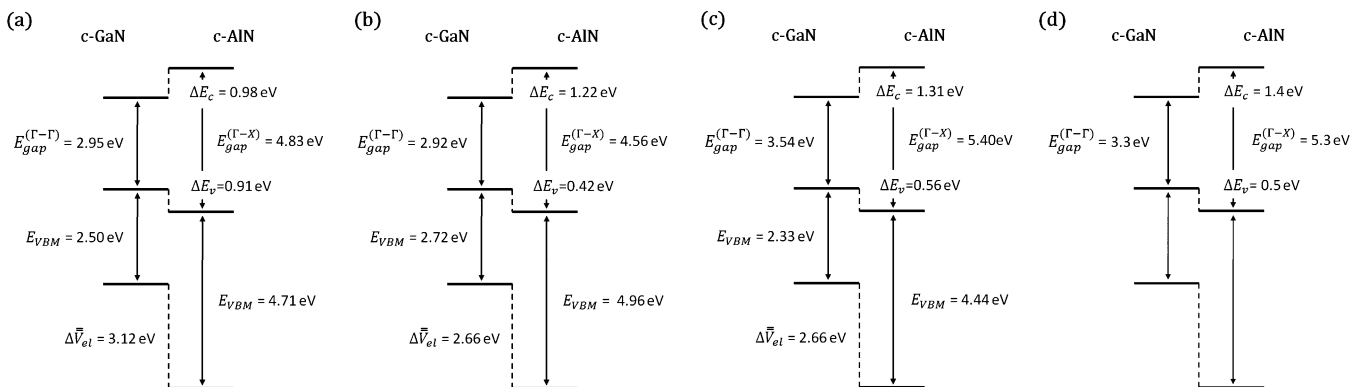


FIG. 8. Schematic of the calculated type-I QP-band alignment for (a) LDA + G_0W_0 , (b) HSE06, (c) HSE06 + G_0W_0 , and (d) experimental results.

and without QP corrections within the *GW* approach, a further analysis of band offsets in heterostructures composed of different technologically relevant semiconductor materials remains necessary.

IV. SUMMARY

High-quality *c*-GaN/AlN SLs were fabricated using PA-MBE. We determined the ratio of CBO to VBO between *c*-GaN and *c*-AlN in our structures by the analysis of ISBT and interband transition energies. For the calculation of ISBT and interband transition energies, the CBO was varied using the structural properties known from HRXRD. Optimal agreement between calculated and experimental data was achieved for a CBO-to-VBO ratio of (74:26)% within an accuracy of $\pm 5\%$ of the band-gap difference ΔE_{gap} .

For all QWs, an energy dependency of effective masses was taken into account to fit the experimental values. These values were verified by the analysis of interband transition energies of our samples in comparison to calculated values using the CBO obtained from inter-sub-band spectroscopy and model calculations.

Furthermore, we have demonstrated that state-of-the-art hybrid-functional DFT calculations and the inclusion of many-body corrections on the G_0W_0 level are able to reproduce the experimental VBO and CBO within 0.1-eV accuracy.

Finally, we conclude that our comprehensive experimental and theoretical results give strong evidence for a CBO of (1.4 ± 0.1) eV and a VBO of (0.5 ± 0.1) eV in *c*-GaN/AlN SL structures.

ACKNOWLEDGMENTS

This work was financially supported by the Deutsche Forschungsgemeinschaft (Projects No. As 107/4-1 and No. SCHM 1361/11-1). The financial support by the EC FET-OPEN program Unitride under Grant No. ga#233950 and the French National Research Agency Project Cosni Grant No. ANR-08-BLAN-0298-01 is acknowledged. The calculations were performed using grants of computer time from the Paderborn Center for Parallel Computing (PC2) and the High Performance Computing Center Stuttgart (HLRS).

-
- ¹H. Machhadani, P. Kandaswamy, S. Sakr, A. Vardi, A. Wirtmüller, L. Nevou, F. Guillot, G. Pozzovivo, M. Tchernycheva, A. Lupu, L. Vivien, P. Crozat, E. Warde, C. Bougerol, S. Schacham, G. Strasser, G. Bahir, E. Monroy, and F. H. Julien, *New J. Phys.* **11**, 125023 (2009).
- ²D. As, *Microelectron. J.* **40**, 204 (2009).
- ³S. V. Novikov, C. T. Foxon, and A. J. Kent, *Phys. Status Solidi A* **207**, 1277 (2010).
- ⁴J. Schörmann, S. Potthast, D. J. As, and K. Lischka, *Appl. Phys. Lett.* **89**, 131910 (2006).
- ⁵T. Schupp, K. Lischka, and D. J. As, *J. Cryst. Growth* **312**, 1500 (2010).
- ⁶E. Tschumak, R. Granzner, J. K. N. Lindner, F. Schwierz, K. Lischka, H. Nagasawa, M. Abe, and D. J. As, *Appl. Phys. Lett.* **96**, 253501 (2010).
- ⁷N. Zainal, S. V. Novikov, C. J. Mellor, C. T. Foxon, and A. J. Kent, *Appl. Phys. Lett.* **97**, 112102 (2010).
- ⁸J. E. A. DeCuir, E. Fred, M. O. Manasreh, J. Schörmann, D. J. As, and K. Lischka, *Appl. Phys. Lett.* **91**, 041911 (2007).
- ⁹H. Machhadani, M. Tchernycheva, S. Sakr, L. Rigutti, R. Colombelli, E. Warde, C. Mietze, D. J. As, and F. H. Julien, *Phys. Rev. B* **83**, 075313 (2011).
- ¹⁰A. Baldereschi, S. Baroni, and R. Resta, *Phys. Rev. Lett.* **61**, 734 (1988).
- ¹¹L. Kleinman, *Phys. Rev. B* **24**, 7412 (1981).
- ¹²O. Brandt, P. Waltereit, and K. H. Ploog, *J. Phys. D* **35**, 577 (2002).
- ¹³nextnano³ device simulator: The program is available at [www.wsi.tum.de/nextnano3 and www.nextnano.de].
- ¹⁴A. Trellakis, T. Zibold, T. Andlauer, S. Birner, R. K. Smith, R. Morschl, and P. Vogl, *J. Comp. Elec.* **5**, 285 (2006).
- ¹⁵S. Birner, S. Hackenbuchner, M. Sabathil, G. Zandler, J. A. Majewski, T. Andlauer, T. Zibold, R. Morschl, A. Trellakis, and P. Vogl, *Acta Phys. Pol. A* **110**, 111 (2006).
- ¹⁶M. Städele and K. Hess, *J. Appl. Phys.* **88**, 6945 (2000).
- ¹⁷E. O. Kane, *J. Phys. Chem. Solids* **1**, 249 (1957).
- ¹⁸C. Wetzel, R. Winkler, M. Drechsler, B. K. Meyer, U. Rössler, J. Scriba, J. P. Kotthaus, V. Härle, and F. Scholz, *Phys. Rev. B* **53**, 1038 (1996).
- ¹⁹M. Röppischer, R. Goldhahn, G. Rossbach, P. Schley, C. Cobet, N. Esser, T. Schupp, K. Lischka, and D. J. As, *J. Appl. Phys.* **106**, 076104 (2009).
- ²⁰V. Bougrov, M. Levinshtein, S. Rumyantsev, and A. Zubrilov, *Properties of Advanced Semiconductor Materials GaN, AlN, InN, BN, SiC, SiGe* (Wiley, New York, 2001).
- ²¹I. Petrov, E. Mojab, R. C. Powell, J. E. Greene, L. Hultman, and J.-E. Sundgren, *Appl. Phys. Lett.* **60**, 2491 (1992).
- ²²M. Mizuta, S. Fujieda, Y. Matsumoto, and T. Kawamura, *Jpn. J. Appl. Phys., Part 2* **25**, L945 (1986).
- ²³S. K. Pugh, D. J. Dugdale, S. Brand, and R. A. Abram, *Semicond. Sci. Technol.* **14**, 23 (1999).
- ²⁴W. J. Fan, M. F. Li, T. C. Chong, and J. B. Xia, *J. Appl. Phys.* **79**, 188 (1996).
- ²⁵C. G. V. de Walle and J. Neugebauer, *Appl. Phys. Lett.* **70**, 2577 (1997).
- ²⁶K. Kim, W. R. L. Lambrecht, and B. Segall, *Phys. Rev. B* **53**, 16310 (1996).
- ²⁷P. Rinke, M. Winkelkemper, A. Qteish, D. Bimberg, J. Neugebauer, and M. Scheffler, *Phys. Rev. B* **77**, 075202 (2008).
- ²⁸J. W. Orton, *Semicond. Sci. Technol.* **12**, 64 (1997).
- ²⁹P. Hohenberg and W. Kohn, *Phys. Rev.* **136**, B864 (1964).
- ³⁰W. Kohn and L. J. Sham, *Phys. Rev.* **140**, A1133 (1965).
- ³¹P. E. Blöchl, *Phys. Rev. B* **50**, 17953 (1994).
- ³²G. Kresse and D. Joubert, *Phys. Rev. B* **59**, 1758 (1999).
- ³³G. Kresse and J. Furthmüller, *Comput. Mater. Sci.* **6**, 15 (1996).
- ³⁴D. M. Ceperley and B. J. Alder, *Phys. Rev. Lett.* **45**, 566 (1980).
- ³⁵J. P. Perdew and A. Zunger, *Phys. Rev. B* **23**, 5048 (1981).

- ³⁶J. Heyd, G. E. Scuseria, and M. Ernzerhof, *J. Chem. Phys.* **118**, 8207 (2003).
- ³⁷J. Heyd and G. E. Scuseria, *J. Chem. Phys.* **121**, 1187 (2004).
- ³⁸J. Heyd, J. E. Peralta, G. E. Scuseria, and R. L. Martin, *J. Chem. Phys.* **123**, 174101 (2005).
- ³⁹J. Heyd, G. E. Scuseria, and M. Ernzerhof, *J. Chem. Phys.* **124**, 219906 (2006).
- ⁴⁰J. P. Perdew, *Int. J. Quantum Chem.* **28**, 497 (1985).
- ⁴¹J. P. Perdew and M. Levy, *Phys. Rev. Lett.* **51**, 1884 (1983).
- ⁴²L. J. Sham and M. Schlüter, *Phys. Rev. Lett.* **51**, 1888 (1983).
- ⁴³O. A. Vydrov and G. E. Scuseria, *J. Chem. Phys.* **121**, 8187 (2004).
- ⁴⁴J. P. Perdew, M. Ernzerhof, and K. Burke, *J. Chem. Phys.* **105**, 9982 (1996).
- ⁴⁵M. Ernzerhof, J. P. Perdew, and K. Burke, *Int. J. Quantum Chem.* **64**, 285 (1997).
- ⁴⁶C. Adamo and V. Barone, *J. Chem. Phys.* **110**, 6158 (1999).
- ⁴⁷M. Ernzerhof and G. E. Scuseria, *J. Chem. Phys.* **110**, 5029 (1999).
- ⁴⁸J. P. Perdew, K. Burke, and M. Ernzerhof, *Phys. Rev. Lett.* **77**, 3865 (1996).
- ⁴⁹A. V. Krukau, O. A. Vydrov, A. F. Izmaylov, and G. E. Scuseria, *J. Chem. Phys.* **125**, 224106 (2006).
- ⁵⁰T. M. Henderson, J. Paier, and G. E. Scuseria, *Phys. Status Solidi B* **248**, 767 (2011).
- ⁵¹J. W. Nicklas and J. W. Wilkins, *Appl. Phys. Lett.* **97**, 091902 (2010).
- ⁵²H.-P. Komsa, P. Broqvist, and A. Pasquarello, *Phys. Rev. B* **81**, 205118 (2010).
- ⁵³However, the admixing of $\frac{1}{4}$ exact exchange has been rationalized by perturbation theory.⁴⁴
- ⁵⁴L. Hedin, *Phys. Rev.* **139**, A796 (1965).
- ⁵⁵L. Hedin and S. Lundqvist, in *Solid State Physics*, edited by F. Seitz, D. Turnbull, and H. Ehrenreich (Academic, New York, 1965), Vol. 23.
- ⁵⁶M. S. Hybertsen and S. G. Louie, *Phys. Rev. B* **32**, 7005 (1985).
- ⁵⁷M. S. Hybertsen and S. G. Louie, *Phys. Rev. B* **34**, 5390 (1986).
- ⁵⁸Details of VASP implementation are given in Refs. 59–62.
- ⁵⁹M. Shishkin and G. Kresse, *Phys. Rev. B* **75**, 235102 (2007).
- ⁶⁰M. Shishkin, M. Marsman, and G. Kresse, *Phys. Rev. Lett.* **99**, 246403 (2007).
- ⁶¹M. Shishkin and G. Kresse, *Phys. Rev. B* **74**, 035101 (2006).
- ⁶²F. Fuchs, J. Furthmüller, F. Bechstedt, M. Shishkin, and G. Kresse, *Phys. Rev. B* **76**, 115109 (2007).
- ⁶³J. Paier, M. Marsman, and G. Kresse, *Phys. Rev. B* **78**, 121201 (2008).
- ⁶⁴H. J. Monkhorst and J. D. Pack, *Phys. Rev. B* **13**, 5188 (1976).
- ⁶⁵T. Lei, T. D. Moustakas, R. J. Graham, Y. He, and S. J. Berkowitz, *J. Appl. Phys.* **71**, 4933 (1992).
- ⁶⁶I. Vurgaftman, J. R. Meyer, and L. R. Ram-Mohan, *J. Appl. Phys.* **89**, 5815 (2001).
- ⁶⁷C. Mietze, E. A. DeCuir, M. O. Manasreh, K. Lischka, and D. J. As, *Phys. Status Solidi C* **7**, 1610 (2010).
- ⁶⁸M. Tchernycheva, L. Nevou, L. Doyennette, F. H. Julien, E. Warde, F. Guillot, E. Monroy, E. Bellet-Amalric, T. Remmele, and M. Albrecht, *Phys. Rev. B* **73**, 125347 (2006).
- ⁶⁹Q. Guo, A. Yoshida, *Jpn. J. Appl. Phys., Part 1* **33**, 2453 (1994).
- ⁷⁰A. F. Wright and J. S. Nelson, *Phys. Rev. B* **51**, 7866 (1995).
- ⁷¹C. Stampfl and C. G. Van de Walle, *Phys. Rev. B* **59**, 5521 (1999).
- ⁷²T. Kotani, M. van Schilfgaarde, and S. V. Faleev, *Phys. Rev. B* **76**, 165106 (2007).
- ⁷³S. Lany and A. Zunger, *Phys. Rev. B* **81**, 113201 (2010).
- ⁷⁴D. Cociorva, W. G. Aulbur, and J. W. Wilkins, *Solid State Commun.* **124**, 63 (2002).
- ⁷⁵E. A. Albanesi, W. R. L. Lambrecht, and B. Segall, *J. Vac. Sci. Technol. B* **12**, 2470 (1994).
- ⁷⁶S.-H. Wei and A. Zunger, *Appl. Phys. Lett.* **72**, 2011 (1998).
- ⁷⁷N. Binggeli, P. Ferrara, and A. Baldereschi, *Phys. Rev. B* **63**, 245306 (2001).